Supplementary Material:

Surface wave tomography for the Pacific Ocean incorporating seafloor seismic observations and plate thermal evolution

T. Isse et al.

S1. Effects of data weighting and results of the checkerboard resolution tests

This study used more seismic stations and events in the western Pacific than in the eastern Pacific Ocean, and, therefore, the ray paths were denser in the former. To rebalance the uneven ray distribution and to account for the relatively small number of phase speed measurements per BBOBS station (as the observation period for BBOBS data is typically ∼1 year), we weighted the Rayleigh wave and Love wave data for events with longitudes greater than 190°E, latitudes outside the range of 50°N–40°S, or data recorded by a BBOBS. We changed the factor from 1.0 to 3.0 and performed the checkerboard resolution tests (Figure S2). When we did not apply weight to the data, the checkerboard patterns were well recovered only in the western Pacific Ocean (Figure S2a and d). In the Rayleigh wave case, the well-recovered regions increased when factors of

2 and 3 were applied (Figure S2b and c). In the Love wave case, applying a factor of 3 was necessary (Figure S2e and f). In our inversion method, we performed ray tracing so that a uniform recovered amplitude was preferable in the eastern and western parts of the Pacific Ocean. Figure S2c (Rayleigh wave, factor of 3) shows that the recovered amplitude was stronger in the eastern part than in the western part and that the regional difference of the recovered amplitude was larger than in the case of a factor of 2. In this study, we chose a factor of 2.0 in the Rayleigh wave data and 3.0 in the Love wave data.

We performed the checkerboard resolution tests to assess the horizontal resolution and the effects of applying different weighting schemes to the data. We calculated the synthetic path-averaged phase speed data from the input checkerboard models incorporating the finite frequency effect, and we subsequently inverted them for the phase speed maps.

Figure S2 shows an example of the results of 8° checkerboard resolution tests with different weights at a period of 83 s. In tests where the data were unweighted, the checkerboard pattern was recovered only in the western Pacific Ocean (Figure S2a and c). In tests where the Rayleigh wave and Love wave data were weighted as described in the main text, the recovered amplitudes of the checkerboard patterns in the eastern Pacific Ocean were improved. The shapes of the checkerboard patterns were well recovered in the western and southeastern parts of the Pacific Ocean. Figure S3 shows the results of the checkerboard resolution tests for the fundamental-mode Love and Rayleigh waves at a period of 83 s with cell sizes of 6° to 16°. Checkerboard patterns were recovered in the entire Pacific Ocean when the cell sizes were larger than 14° and 18°, and in the western Pacific Ocean at cell sizes of 6° and 10° for the Rayleigh waves and Love waves, respectively. In the present study, the lateral resolution of the isotropic structure in the entire Pacific Ocean was ~15° and that in the western Pacific Ocean was ~8°. The lateral resolution of the radially anisotropic structure was worse because of the worse recovery of the checkerboard pattern in the Love wave test. The resolution was ~18° in the entire Pacific Ocean and ~10° in the western Pacific Ocean. The different spatial resolution in the Love and Rayleigh waves may affect the radially anisotropic structure. When we simply made radial anisotropy maps, there were many small-scale anomalies below the spatial resolution, which were randomly distributed in the entire Pacific Ocean. To diminish these small-scale anomalies, we applied a spatial low-pass filter at 15° for the isotropic structure and 18° for the radially anisotropic structure to the results discussed in the context of the entire Pacific region and at 8° and 10° for the western Pacific region.

S2 Jackknife error estimation

Understanding the trade-off between the model resolution and error is helpful for interpreting inversion results. Panning and Romanowicz (2006) suggested that the bootstrap or jackknife error estimation was useful for the purpose and that estimated errors of both methods were virtually identical. Applying the bootstrap method to this study is not practical due to heavy computation, and thus we apply the jackknife error estimation.

We divide the original data into 10 subsets by random selection without duplication and then construct 10 jackknife data samples by removing one of the subsets from the original data. We calculate a phase-speed map for each of those jackknife samples. The average and standard errors are estimated following Panning and Romanowicz (2006) (Figure S12). The estimated errors are less than 0.02 km/s for the fundamental mode surface wave, and 0.05 km/s for higher modes. Large errors can be seen along the Pacific rim for higher modes, whereas errors are small in most of the

Pacific Ocean. The estimated errors of the phase speed maps are small enough to be used to construct local shear wave speed models.

Panning, M., Romanowicz, B., 2006. A three-dimensional radially anisotropic model of shear velocity in the whole mantle. Geophys. J. Int. 167, 361–379. doi:10.1111/j.1365-246X.2006.03100.x

Supplemental Figure Captions

Figure S1

Plot of the ray distribution of fundamental-mode (a) Rayleigh and (b) Love waves at a period of 83 s. Red lines indicate rays observed by BBOBSs. Blue triangles indicate BBOBS locations. Finite-width ray densities of the (c) Rayleigh and (d) Love waves. We counted the cells that were covered by the influence zone.

Figure S2

Result of the checkerboard resolution tests for fundamental-mode surface waves at a period of 83 s using 10° cells to assess the effects of different weighting schemes on the data. (a) Result of the checkerboard resolution test for Rayleigh waves with no weighting scheme. (b) Result of the checkerboard resolution test for Rayleigh waves assigned a weight of 2.0. (c) Result of the checkerboard resolution test for Rayleigh waves assigned a weight of 3.0. (d–f) Same as for (a–c) but with Love waves. Recovered amplitudes in the eastern half of the Pacific Ocean were improved relative to the no-weighting scheme.

Figure S3

Results of the checkerboard resolution tests for fundamental-mode surface waves at a period of 83 s with (a, e) 6°, (b, f) 8°, (c, g) 12°, and (d, h) 16° cells for (a–d) Love and (e–h) Rayleigh waves.

Figure S4

(a) Age-bin-averaged β_{iso} and (b) age-bin-averaged radial anisotropy profiles of the Pacific Plate regions from the PAC-c model. In (a), the thin black contour lines show shear-wave speeds at 0.05 km/s intervals, whereas the thick black line shows the 1100 °C isotherms of the HSC model used in the modeling.

Figure S5

β_{iso} as a function of the geotherm based on the HSC model at 5-Myr intervals from the PAC-c model. Solid circles show the data at ages between 35 and 80 Ma, from which we estimated the thermal coefficient of β_{iso}. Solid lines show the predicted shear-wave speed profiles calculated with the equations shown in the figure. Different colors correspond to different depths.

Figure S6

Isotropic shear-wave speed maps of the PA-c model (a–c), PA-age model (d–f), and their difference (g–i) at depths of 50, 75, and 100 km, respectively.

Figure S7

Comparison between the PAC-age model and the previous models of $\delta\beta_{iso}$ (%) at depths of 50, 100, and 200 km.

Figure S8

Same as for Figure S7 but with radial anisotropy.

Figure S9

Results of the synthetic tests for estimating the depths of the negative peaks of the vertical gradient of β_{iso}. Red, blue, and black lines show the speed profiles of the β_{SV}, β_{SH}, and β_{iso}, respectively. Broken lines show the input models, whereas solid lines show the recovered models. The discontinuity depths of the input models are indicated by black arrows at (a) 50, (b) 60, (c) 90, (d) 120, and (e) 140 km, respectively. (f) Comparisons between the recovered negative peak depths and the input discontinuity depths for β_{SV}, β_{SH}, and β_{iso}.

Figure S10

Comparison between (a–c) PAC-age, (d–f) PAC-age-exOBS, and (g–i) their difference at depths of 50, 100, and 200 km, respectively.

Figure S11

Same as for Figure 10 but using the plate model of Parsons and Sclater (1977) to estimate the mantle temperature.

Figure S12

Standard errors of phase speeds calculated by using a jackknife approach for the fundamental mode surface wave at periods of 50 and 100s (left and middle), and the first higher mode at a period of 100 s (right). Upper panels show the results for Love wave and lower panels for Rayleigh wave.

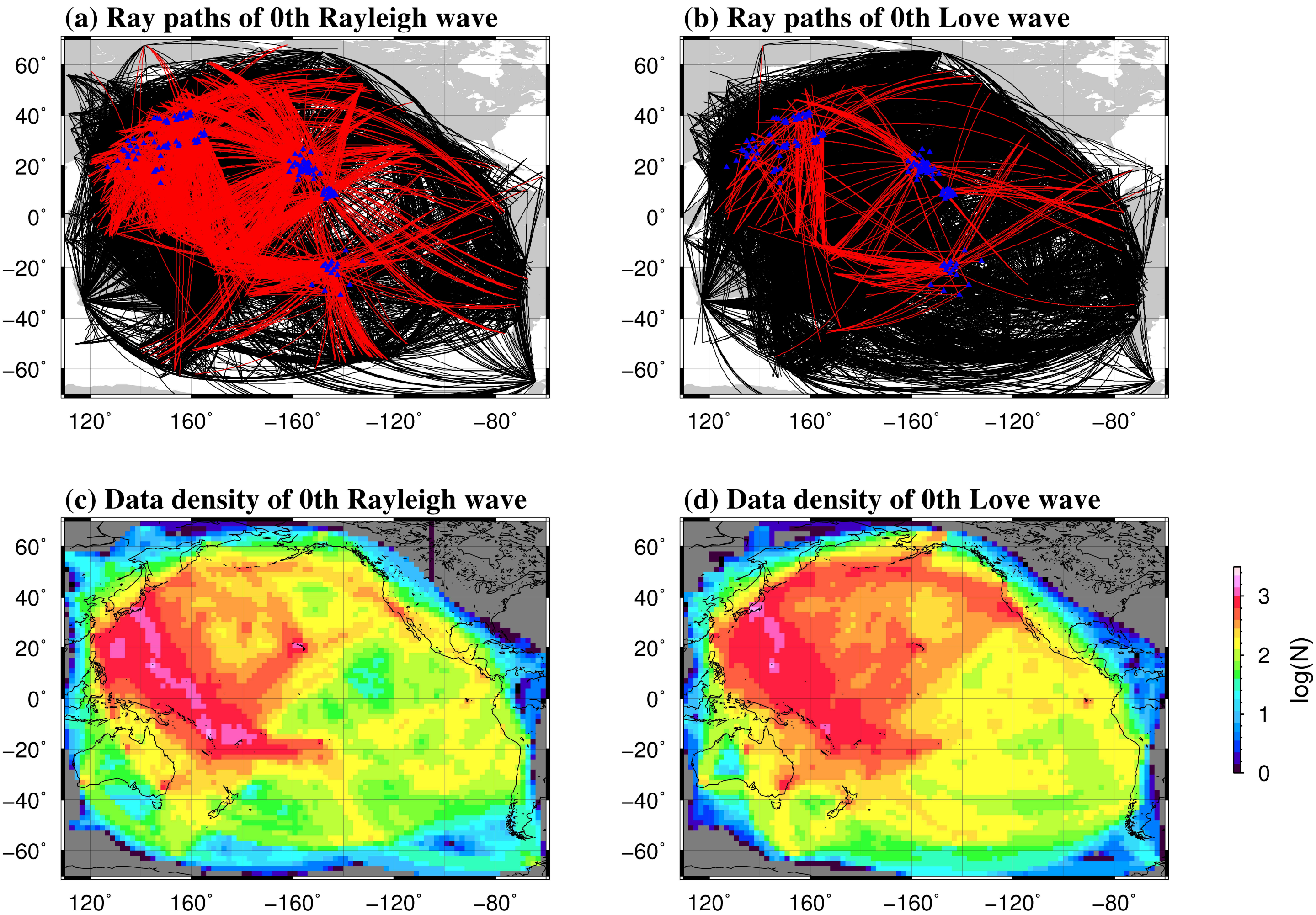
(a) Ray paths of 0th Rayleigh wave
(b) Ray paths of 0th Love wave
(c) Data density of 0th Rayleigh wave
(d) Data density of 0th Love wave
60˚
40˚
20˚
0˚
−20˚
−40˚
−60˚
120˚
160˚
−160˚
−120˚
−80˚
log(N)
0
1
2
3

Figure S1

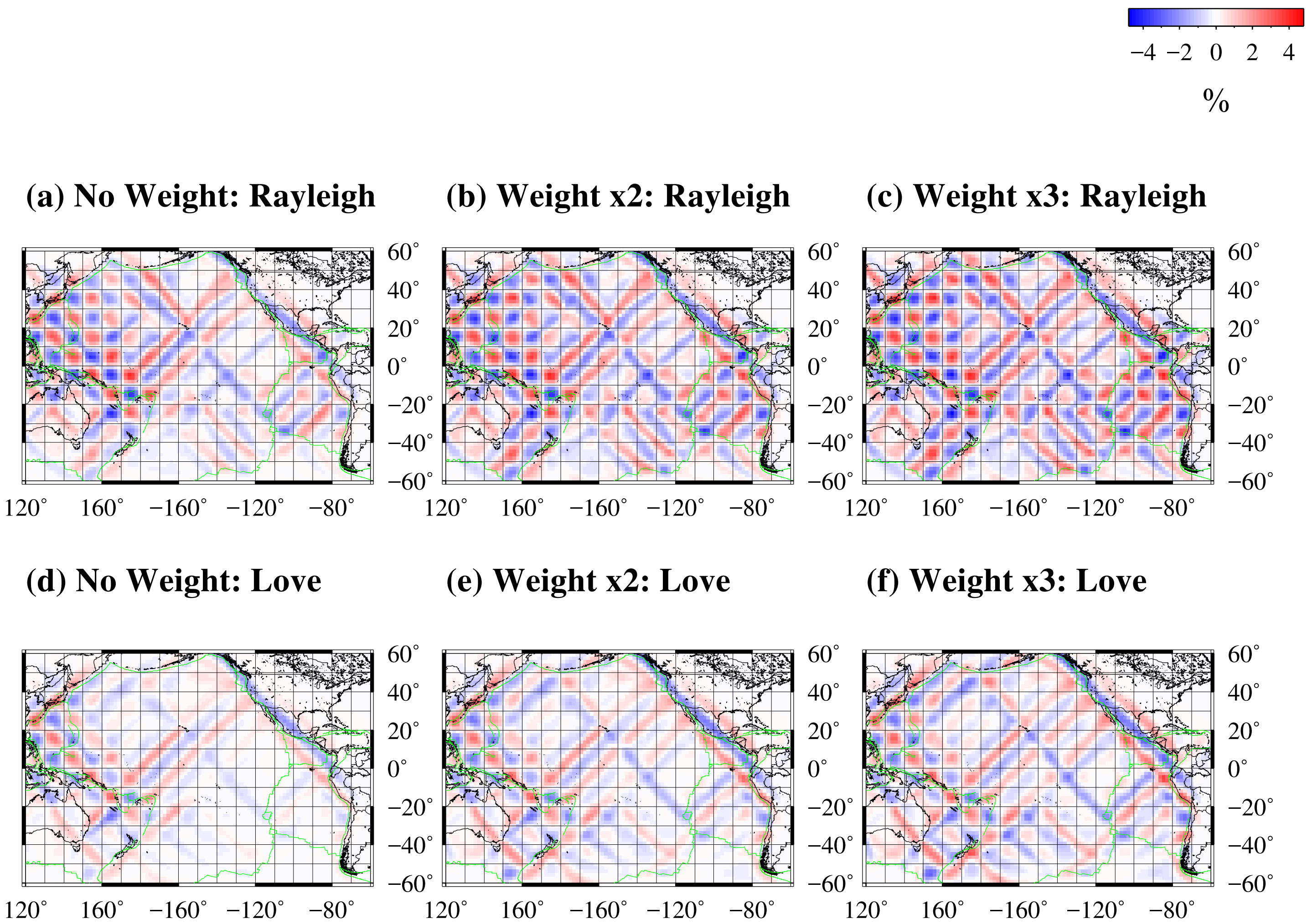

−4 −2 0 2 4
%
(a) No Weight: Rayleigh
(b) Weight x2: Rayleigh
(c) Weight x3: Rayleigh
(d) No Weight: Love
(e) Weight x2: Love
(f) Weight x3: Love
60° 40° 20° 0° −20° −40° −60°
120° 160° −160° −120° −80°

Figure S2

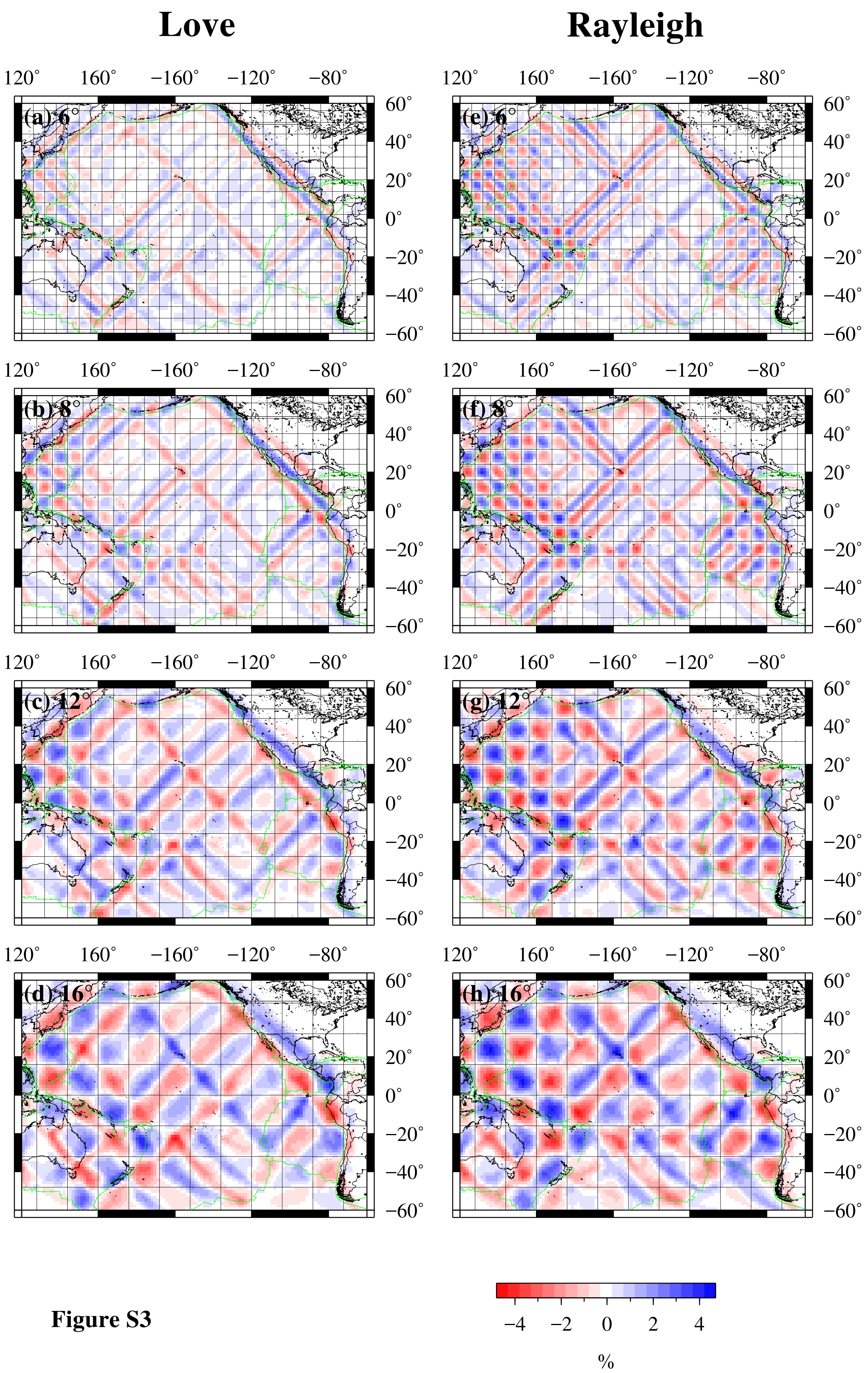
Love
Rayleigh
(a) 6°
(b) 8°
(c) 12°
(d) 16°
(e) 6°
(f) 8°
(g) 12°
(h) 16°
120°
160°
−160°
−120°
−80°
60°
40°
20°
0°
−20°
−40°
−60°
−4
−2
0
2
4
%

Figure S3

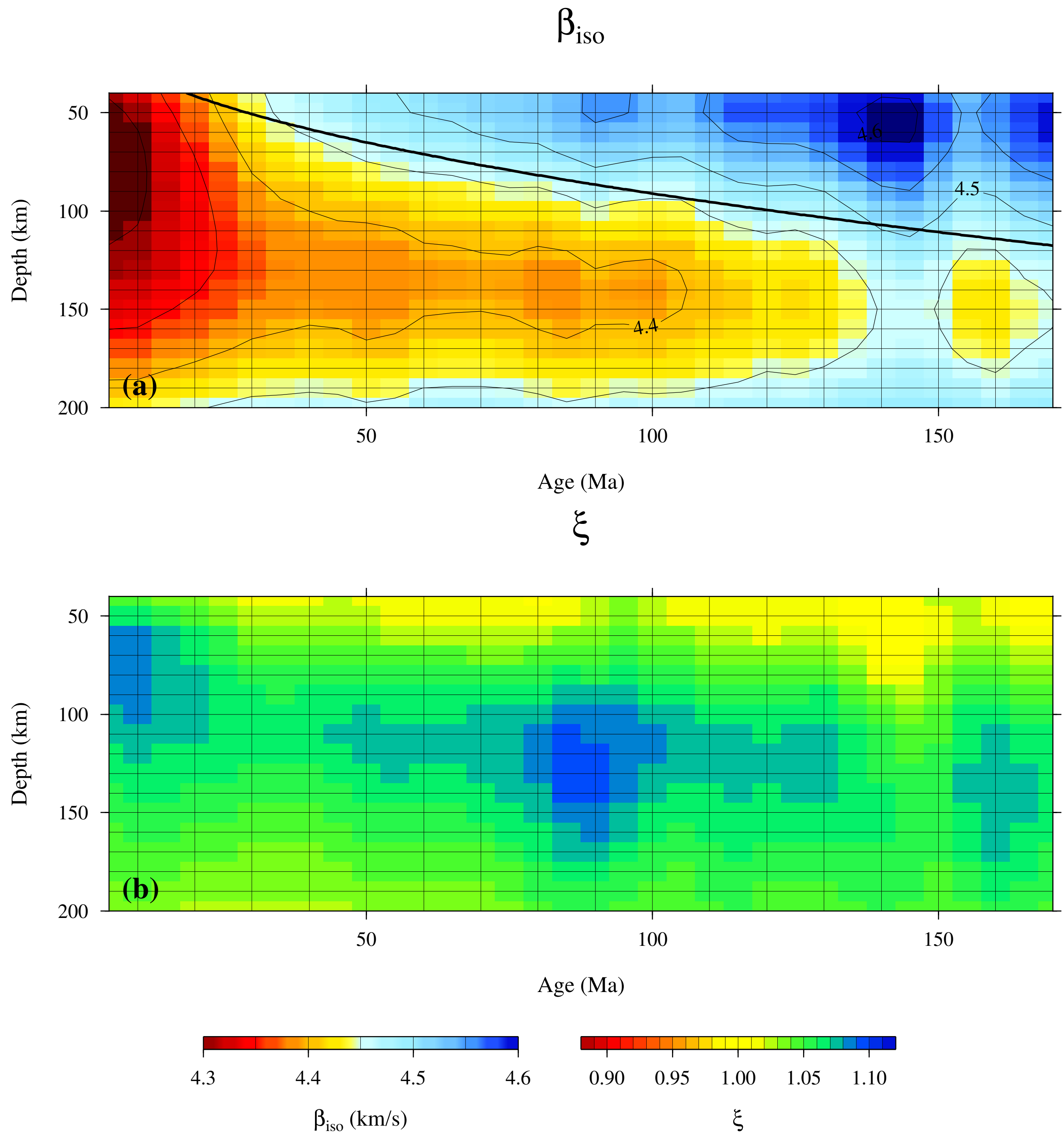

β_{iso}
Depth (km)
50
100
150
200
4.6
4.5
4.4
(a)
50
100
150
Age (Ma)
ξ
Depth (km)
50
100
150
200
(b)
50
100
150
Age (Ma)
4.3
4.4
4.5
4.6
β_{iso} (km/s)
0.90
0.95
1.00
1.05
1.10
ξ

Figure S4

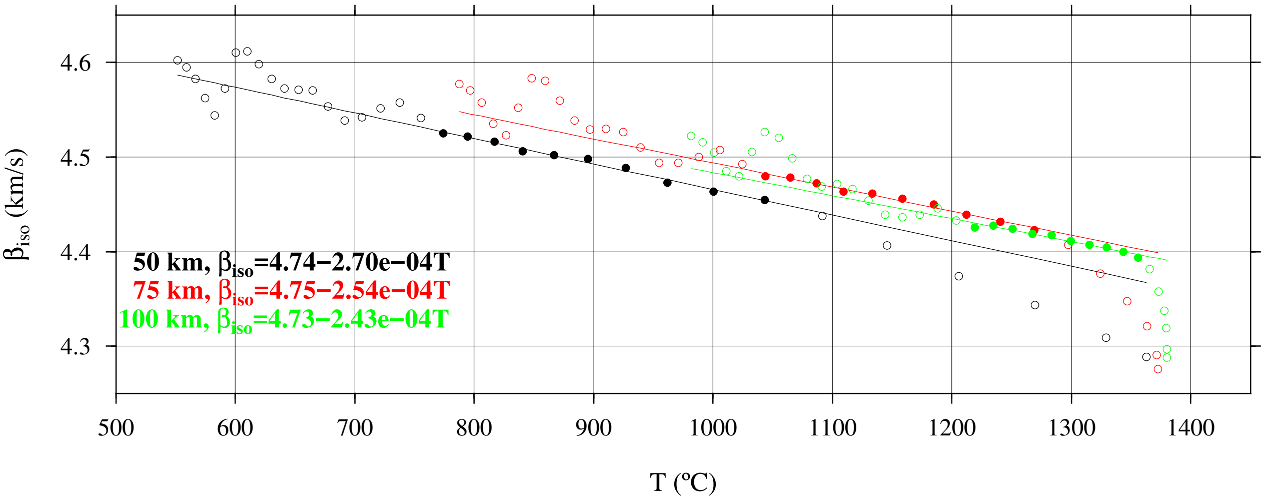

4.6
4.5
4.4
4.3
β_{iso} (km/s)
50 km, β_{iso}=4.74−2.70e−04T
75 km, β_{iso}=4.75−2.54e−04T
100 km, β_{iso}=4.73−2.43e−04T
500
600
700
800
900
1000
1100
1200
1300
1400
T (ºC)

Figure S5

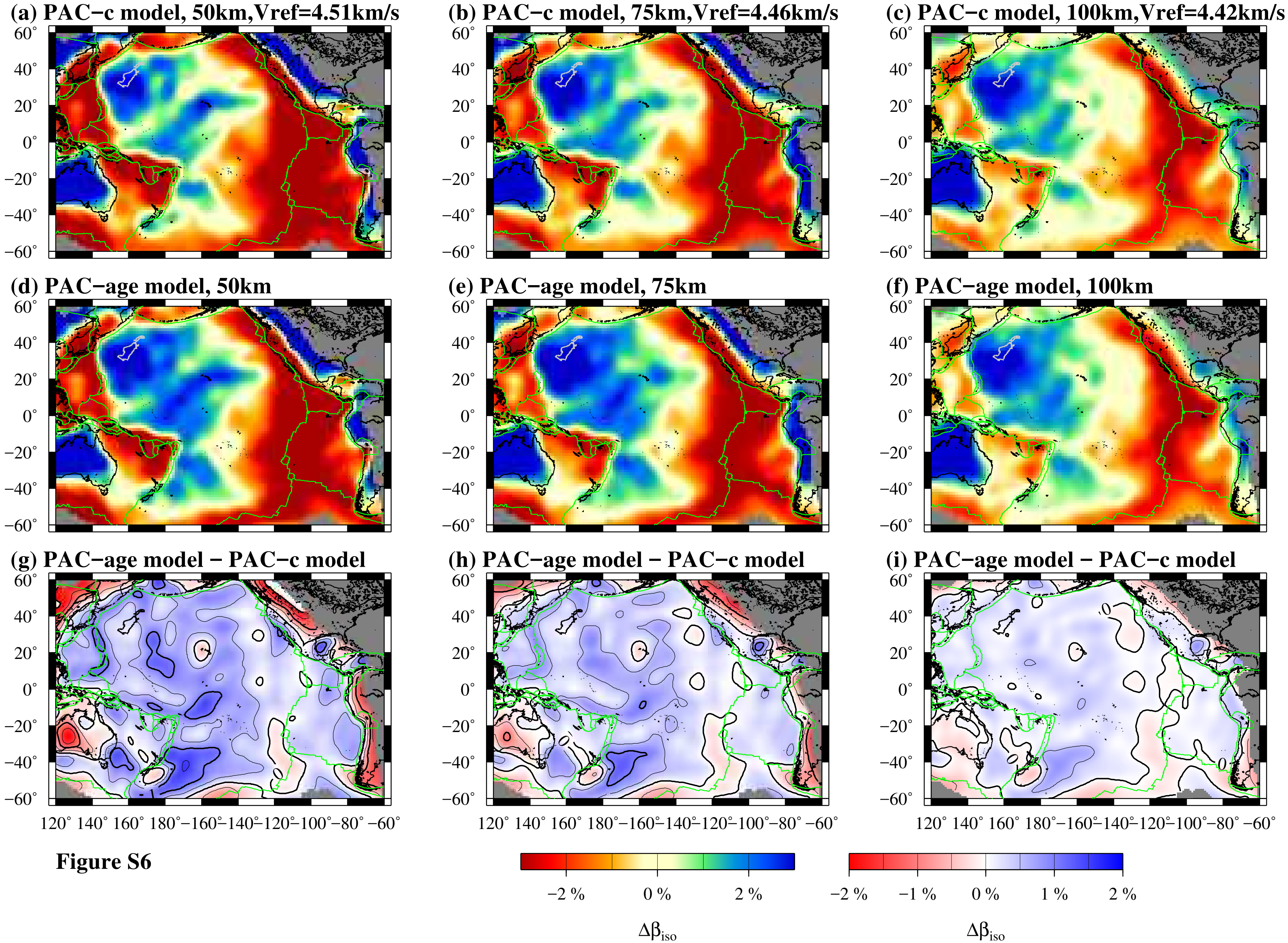

(a) PAC−c model, 50km,Vref=4.51km/s
(b) PAC−c model, 75km,Vref=4.46km/s
(c) PAC−c model, 100km,Vref=4.42km/s
(d) PAC−age model, 50km
(e) PAC−age model, 75km
(f) PAC−age model, 100km
(g) PAC−age model − PAC−c model
(h) PAC−age model − PAC−c model
(i) PAC−age model − PAC−c model
60° 40° 20° 0° −20° −40° −60°
120° 140° 160° 180° −160° −140° −120° −100° −80° −60°
−2 % 0 % 2 %
$\Delta\beta_{iso}$
−2 % −1 % 0 % 1 % 2 %
$\Delta\beta_{iso}$

Figure S6

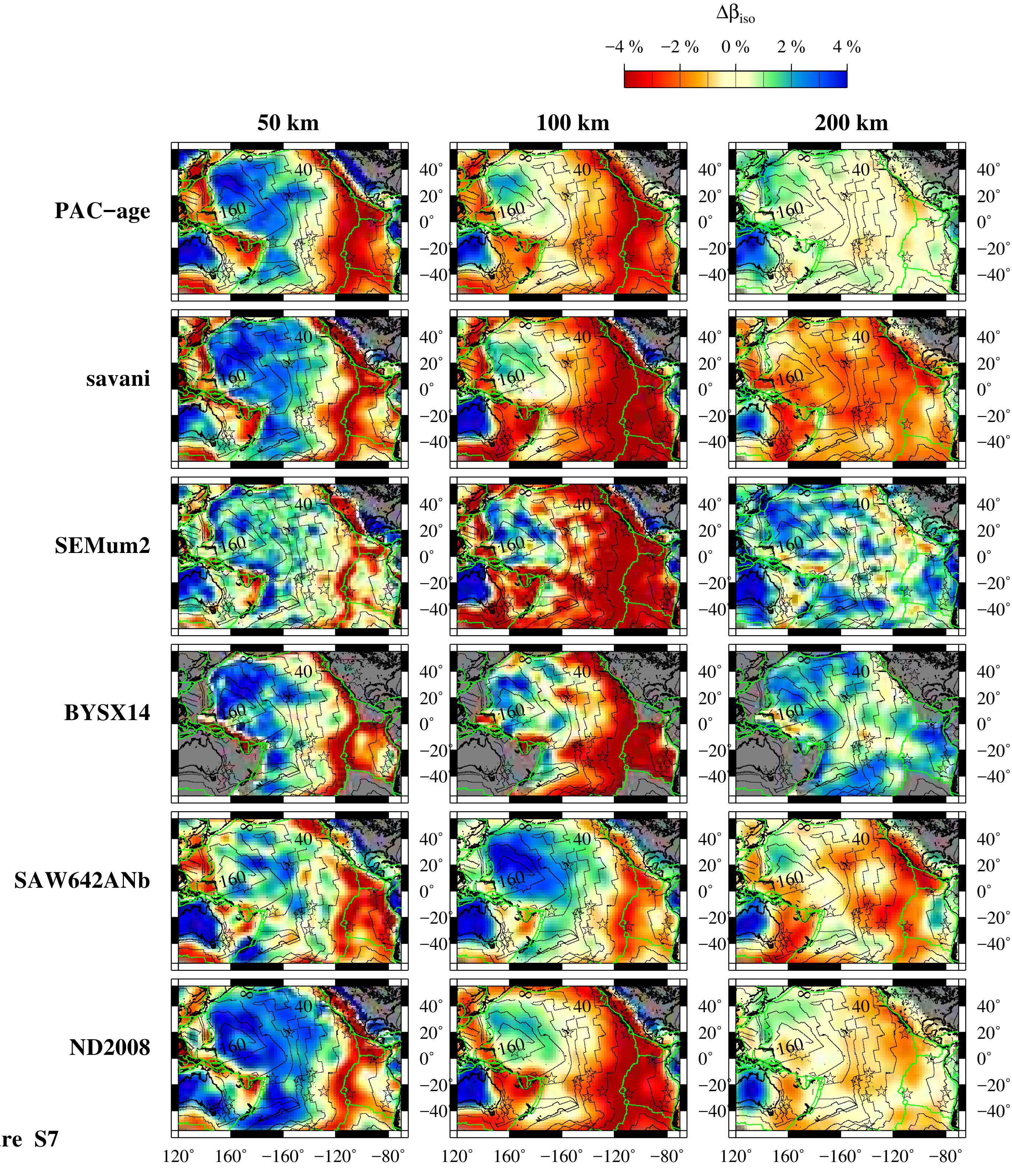

Δβ_iso
−4 %
−2 %
0 %
2 %
4 %
50 km
100 km
200 km
PAC−age
savani
SEMum2
BYSX14
SAW642ANb
ND2008
40°
20°
0°
−20°
−40°
120°
160°
−160°
−120°
−80°
40
160

Figure S7

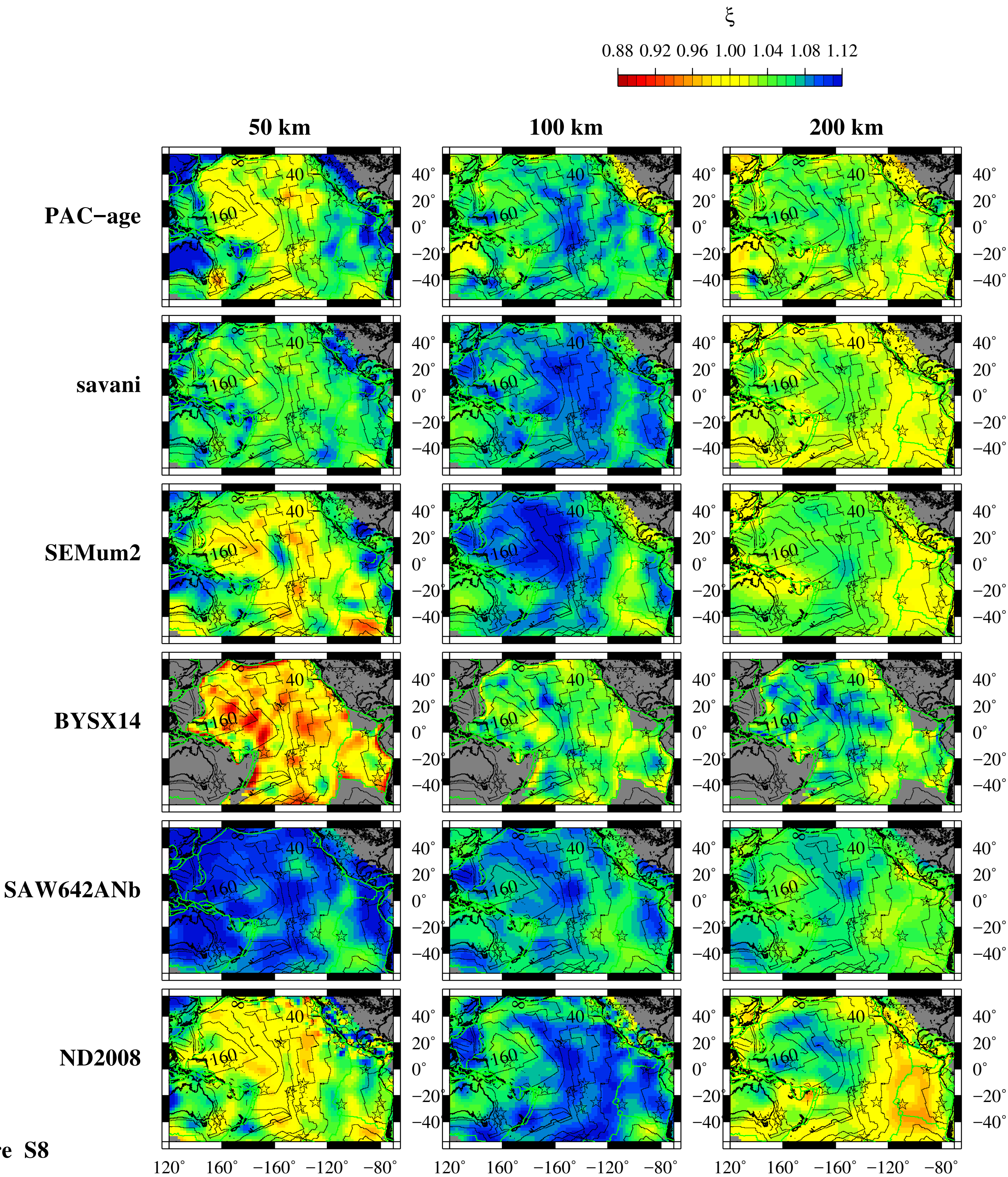
ξ
0.88 0.92 0.96 1.00 1.04 1.08 1.12
50 km
100 km
200 km
PAC−age
savani
SEMum2
BYSX14
SAW642ANb
ND2008
40°
20°
0°
−20°
−40°
120° 160° −160° −120° −80°

Figure S8

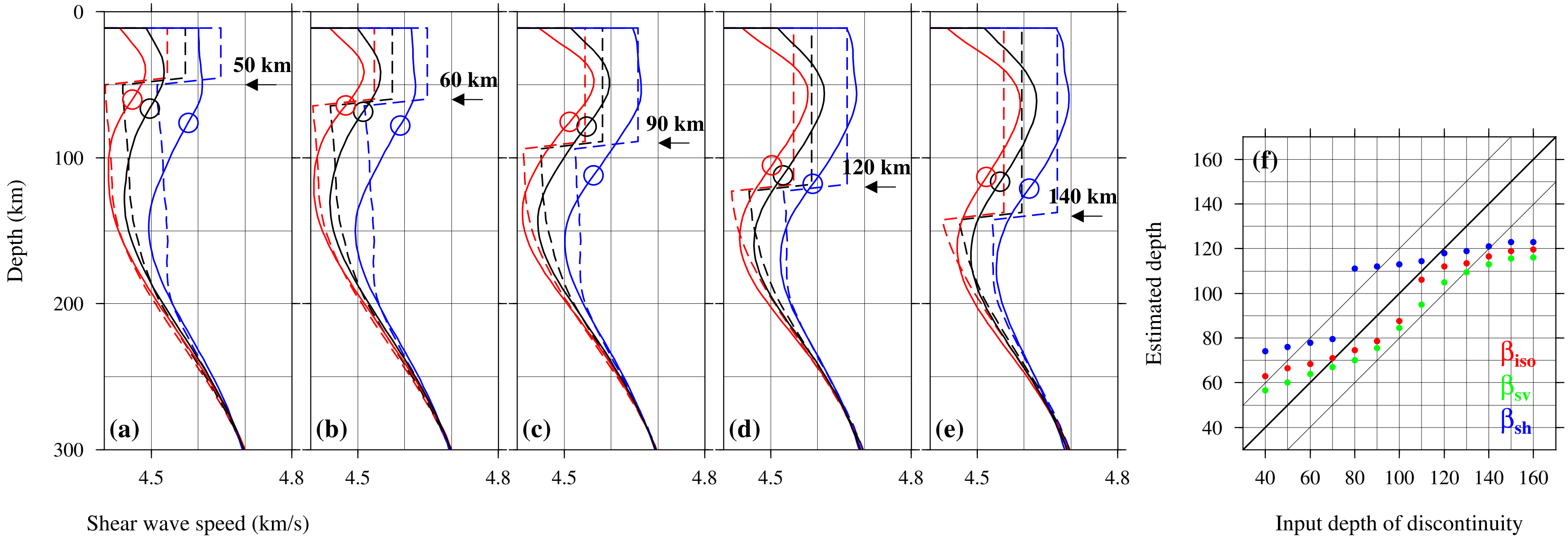

Depth (km)
0
100
200
300
50 km
60 km
90 km
120 km
140 km
(a)
(b)
(c)
(d)
(e)
4.5
4.8
Shear wave speed (km/s)
(f)
Estimated depth
Input depth of discontinuity
40
60
80
100
120
140
160
β_{iso}
β_{sv}
β_{sh}

Figure S9

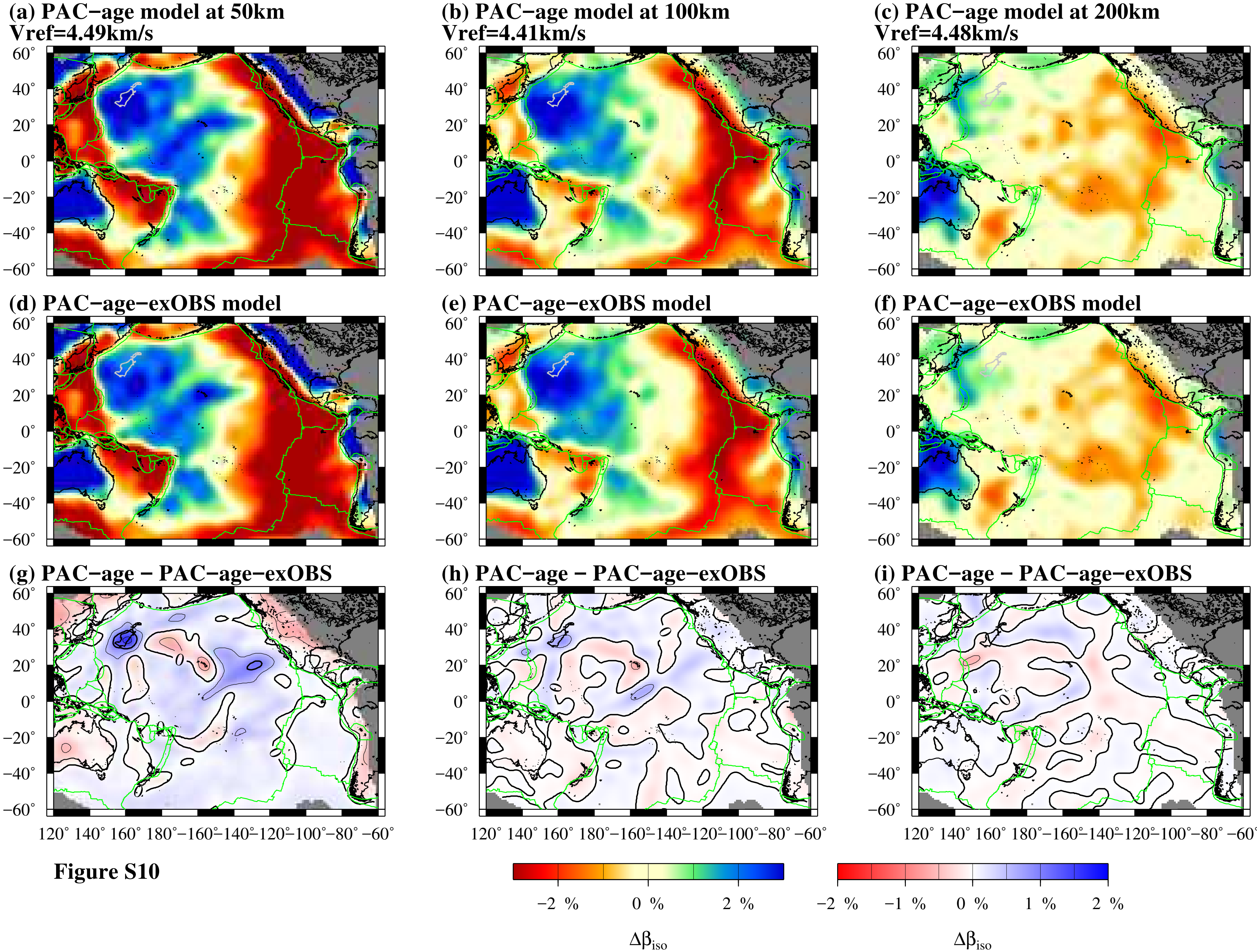
(a) PAC−age model at 50km
Vref=4.49km/s
(b) PAC−age model at 100km
Vref=4.41km/s
(c) PAC−age model at 200km
Vref=4.48km/s
(d) PAC−age−exOBS model
(e) PAC−age−exOBS model
(f) PAC−age−exOBS model
(g) PAC−age − PAC−age−exOBS
(h) PAC−age − PAC−age−exOBS
(i) PAC−age − PAC−age−exOBS
60° 40° 20° 0° −20° −40° −60°
120° 140° 160° 180° −160° −140° −120° −100° −80° −60°
−2 % 0 % 2 %
$\Delta\beta_{iso}$
−2 % −1 % 0 % 1 % 2 %
$\Delta\beta_{iso}$

Figure S10

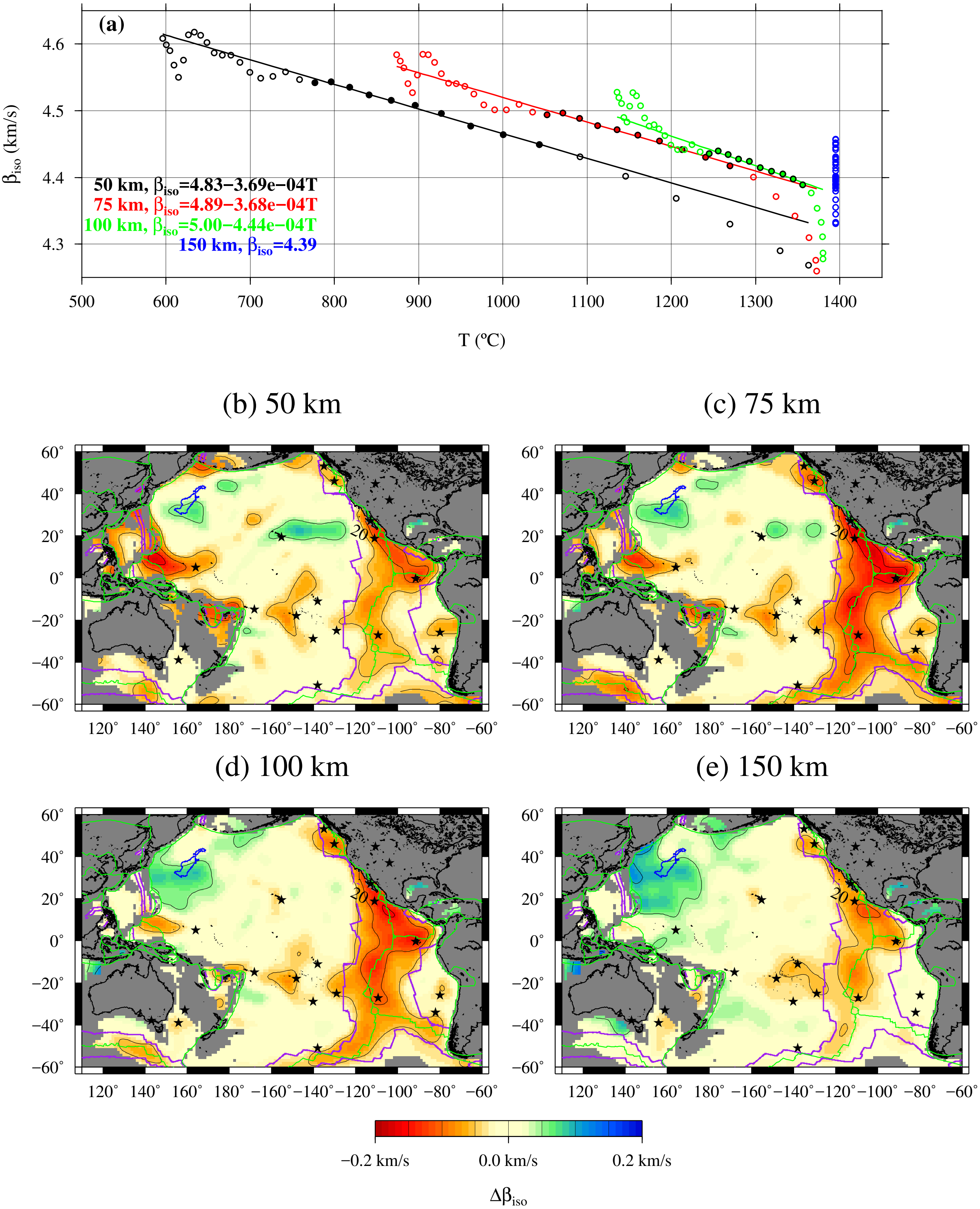

(a)
50 km, βiso=4.83−3.69e−04T
75 km, βiso=4.89−3.68e−04T
100 km, βiso=5.00−4.44e−04T
150 km, βiso=4.39
βiso (km/s)
T (ºC)
(b) 50 km
(c) 75 km
(d) 100 km
(e) 150 km
−0.2 km/s
0.0 km/s
0.2 km/s
Δβiso

Figure S11

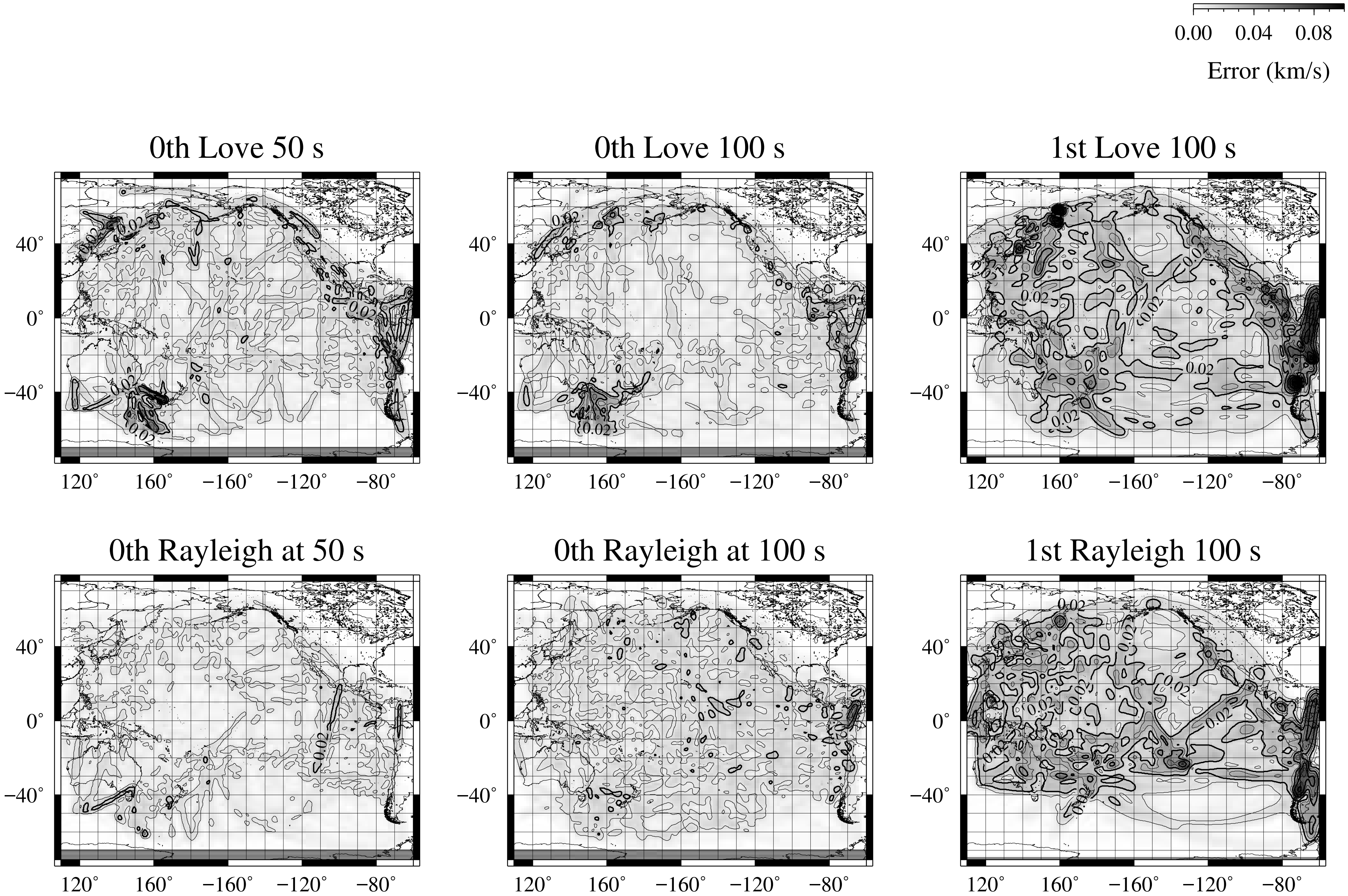

0.00 0.04 0.08
Error (km/s)
0th Love 50 s
0th Love 100 s
1st Love 100 s
0th Rayleigh at 50 s
0th Rayleigh at 100 s
1st Rayleigh 100 s
40°
0°
−40°
120° 160° −160° −120° −80°

Figure S12